In-situ dosage of Fe^{2+} catalyst using natural pyrite for thiamphenicol mineralization by photoelectro-Fenton process

Abdoulaye Thiam,[a] Ricardo Salazar,[b] Enric Brillas,[c] Ignasi Sirés,[c,*]

[a] *Programa Institucional de Fomento a la I+D+i, Universidad Tecnológica Metropolitana, Ignacio Valdivieso 2409, P.O. Box 8940577, San Joaquín, Santiago, Chile*

[b] *Laboratorio de Electroquímica del Medio Ambiente, LEQMA, Facultad de Química y Biología, Universidad de Santiago de Chile, USACh, Casilla 40, Correo 33, Santiago, Chile*

[c] *Laboratori d'Electroquímica dels Materials i del Medi Ambient, Departament de Química Física, Universitat de Barcelona, Martí i Franquès 1-11, 08028 Barcelona, Spain*

*Corresponding author: E-mail: i.sires@ub.edu (I. Sirés)

Abstract

The degradation of the antibiotic thiamphenicol has been studied by photoelectro-Fenton (PEF) process with UVA light using pyrite particles as catalyst source. Pyrite is a sulfide mineral that naturally acidifies the reaction medium and releases Fe^{2+}, thus promoting the effective generation of $^{\bullet}OH$ from Fenton's reaction. The assays were made in an IrO_2/air-diffusion cell, which yielded similar results to a boron-doped diamond (BDD)/air-diffusion one at a lower cost. In dark conditions, electro-Fenton (EF) process showed an analogous ability for drug removal, but mineralization was much poorer because of the large persistence of highly stable by-products. Their photolysis explained the higher performance of PEF. Conventional homogeneous PEF directly using dissolved Fe^{2+} exhibited a lower mineralization power. This suggests the occurrence of heterogeneous Fenton's reaction over the pyrite surface. The effect of current density and drug content on pyrite-catalyzed PEF performance was examined. The drug heteroatoms were gradually converted into SO_4^{2-}, Cl^- and NO_3^- ions. Nine aromatic derivatives and two dichloroaliphatic amines were identified by GC-MS, and five short-chain carboxylic acids were detected by ion-exclusion HPLC. A reaction route for thiamphenicol mineralization by PEF process with continuous H_2O_2 and Fe^{2+} supply on site is proposed.

Keywords: Antibiotic; Catalyst dosage; Electrochemical technology; Emerging contaminants; Heterogeneous photoelectro-Fenton; Water treatment

1. Introduction

Freshwater contains a large number of pharmaceuticals and their metabolites, as a result of their wide use in veterinary and human medicine. These residues are classified as organic micropollutants with a negative impact on the aquatic ecosystems and humans even at trace level (Brillas and Sirés, 2015; Ebele et al., 2017; Miller et al., 2018; da Silva et al., 2019). Pharmaceuticals are also considered as emerging contaminants because their presence in the environment is still unregulated. Their occurrence in freshwater can be mainly associated to poor destruction upon the application of conventional physicochemical and biological methods in municipal wastewater treatment facilities (WWTFs), being ubiquitous in discharged effluents (Prieto-Rodríguez et al., 2013; Campos-Mañas et al., 2017; Kümmerer et al., 2018; Mezzelani et al., 2018). Currently, there is global consensus on the need of advanced technologies for drug removal from water. Among them, considerable research efforts have been focused on some particularly powerful oxidation methods, which show high ability for the quick and total destruction of such pollutants even in secondary effluents (Feng et al., 2013; Brillas and Sirés, 2015; Ye et al., 2020).

Thiamphenicol ($C_{12}H_{15}Cl_2NO_5S$, M = 356,223 g mol^{-1}) is an amphenicol antibiotic for veterinary applications, although it is also used for humans in several countries. It is more potent than chloramphenicol, being also safer since it has not been related to aplastic anemia. Thiamphenicol is used against a wide range of bacterial infections of the gastrointestinal and respiratory tract but, since it is hardly metabolized, its occurrence in water matrices like drinking water has been reported at concentrations up to 101 μg L^{-1} (Chu et al., 2016b; Liu et al., 2019). The removal of thiamphenicol from synthetic and natural water has been successfully achieved by adsorption on granular activated carbon (Fan et al., 2019), and UV or UV/Vis photodegradation (Ge et al., 2009, Li et al., 2014; Liu et al., 2015a). Various advanced oxidation processes (AOPs), whose key feature is the generation of hydroxyl radical ($^{\bullet}OH$) on site, have

also been tested, including UV/Fe(II) (Liu et al., 2015a), UV/H_2O_2 (Liu et al., 2015a; Wang et al., 2017; Yin et al., 2018), UV/persulfate (Chu et al., 2016a; Wang et al., 2017) and UV/CaO_2 (Zheng et al., 2019). In contrast, much less is known about the performance of the electrochemical technologies, only being reported the efficient electrodechlorination of thiamphenicol using a cathode modified with multi-walled carbon nanotubes (Deng et al., 2017).

The electrochemical AOPs (so-called EAOPs) based on H_2O_2 electrogeneration, like electro-oxidation with electrogenerated H_2O_2 (EO-H_2O_2), electro-Fenton (EF) and photoelectro-Fenton (PEF) have recently experienced an impressive development for the treatment of biorecalcitrant organic pollutants (Feng et al., 2013; Sirés et al., 2014; Brillas and Sirés, 2015; da Silva et al., 2019). This set of technologies is particularly well suited for water treatment due to the inherent simplicity and safe conditions, high effectiveness and easy scale-up. The cathodic H_2O_2 production is achieved via the two-electron reduction of O_2, bubbled through the solution or directly fed to a gas chamber, following reaction (1). Cheap carbonaceous materials, like reticulated vitreous carbon (Coria et al., 2015) or carbon felt (Panizza and Oturan, 2011; Ganzenko et al., 2018; Yang et al., 2019; Ye et al., 2019) immersed in the solution, as well as carbon-supported air-diffusion electrodes (Galia et al., 2016; Lanzalaco et al., 2017; Pérez et al., 2017; Ye et al., 2020) are viable for reaction (1).

$$O_{2(g)} + 2H^+ + 2e^- \rightarrow H_2O_2 \quad (1)$$

In EO-H_2O_2, the organic molecules are preeminently destroyed by adsorbed hydroxyl radicals, denoted as M($^\bullet$OH), originated from water discharge at the anode M via reaction (2). Boron-doped diamond (BDD) thin films are preferred because they possess much higher oxidation ability as compared to conventional anodes like DSA® (dimensionally stable anode) and Pt (Boye et al., 2002; Marselli et al., 2003; Panizza and Cerisola, 2009; Scialdone et al., 2011; Thiam et al., 2015; Steter et al., 2016).

$$M + H_2O \rightarrow M(^{\bullet}OH) + H^+ + e^- \quad (2)$$

In homogeneous EF process, a small amount of dissolved Fe^{2+} causes the decomposition of electrogenerated H_2O_2, dramatically enhancing the decontamination due to the production of free $^{\bullet}OH$ in the whole volume via Fenton's reaction (3) (Sirés et al., 2014; Brillas and Sirés, 2015; Galia et al., 2016). The continuous $^{\bullet}OH$ production is favored through the concomitant cathodic reduction of Fe^{3+} to Fe^{2+} by reaction (4). In EF, the nature of the anode has a minor effect, unless recalcitrant reaction intermediates like complexes between Fe(III) and short-chain linear carboxylic acids are formed. In such case, BDD is still preferred because BDD($^{\bullet}OH$) produced from reaction (2) allows their electrocatalytic degradation (Alcaide et al., 2020). Alternatively, the quick photolysis of Fe(III)-carboxylate complexes via reaction (5) upon UV irradiation in homogeneous PEF may also yield a quantitative mineralization (Pérez et al., 2017; Alcaide et al., 2020). This latter process also improves the Fe^{2+} regeneration and $^{\bullet}OH$ production thanks to photo-Fenton reaction (6), usually ending in a larger destruction of organics (Thiam et al., 2015: Steter et al., 2016). The high oxidation power of PEF allows using the less expensive DSA® anode, as for example the IrO_2-based one.

$$Fe^{2+} + H_2O_2 \rightarrow Fe^{3+} + {}^{\bullet}OH + OH^- \quad (3)$$

$$Fe^{3+} + e^- \rightarrow Fe^{2+} \quad (4)$$

$$[Fe(OOCR)]^{2+} + h\nu \rightarrow Fe^{2+} + CO_2 + R^{\bullet} \quad (5)$$

$$[Fe(OH)]^{2+} + h\nu \rightarrow Fe^{2+} + {}^{\bullet}OH \quad (6)$$

Although the homogeneous EF and PEF treatments are optimal at pH ~ 3, the use of heterogeneous iron-rich catalysts has been recently addressed, aiming to manage aqueous solutions at their natural pH (Ganiyu et al., 2018). Natural and synthetic iron oxides (Expósito et al., 2007; Özcan et al., 2017) and mineral pyrite (FeS_2) have shown promising results. In

particular, pyrite has been confirmed as an excellent candidate for heterogeneous Fenton (Liu et al., 2015b; Zhang et al., 2015, 2018) or EF (Barhoumi et al., 2015; Ouiriemmi et al., 2017). It releases Fe^{2+} and H^+ upon conversion of its sulfide group into sulfate via reactions (7) and (8), leading to the occurrence of two $^{\bullet}OH$-mediated routes for the degradation of pollutants: (i) the homogeneous one, based on Fenton's reaction (3), and (ii) the heterogeneous one, arising from the surface decomposition of H_2O_2 via heterogeneous Fenton's reaction (9) (He et al., 2016). However, the potential benefits derived from simultaneous solution irradiation with UV light in the pyrite-catalyzed treatment have not been explored yet.

$$2FeS_2 + 7O_2 + 2H_2O \leftrightarrows 2Fe^{2+} + 4SO_4^{2-} + 4H^+ \quad (7)$$

$$FeS_2 + 14Fe^{3+} + 8H_2O \rightarrow 15Fe^{2+} + 2SO_4^{2-} + 16H^+ \quad (8)$$

$$Fe(II) + H_2O_2 \rightarrow Fe(III) + {}^{\bullet}OH + OH^- \quad (9)$$

This work aims to assess the positive impact of UVA light on the pyrite-catalyzed Fenton-based treatment of thiamphenicol solutions in sulfate medium, employing an electrolytic cell equipped with either an IrO_2 or BDD anode and an air-diffusion cathode. The performance of homogeneous EF and PEF processes was also evaluated to demonstrate the potential advantages of pyrite over a soluble iron salt. The effect of pyrite content and current density (j) on the performance of heterogeneous PEF, as well as the mineral recyclability, were studied. A reaction route for the drug mineralization by heterogeneous EF and PEF processes is proposed from the products identified.

2. Experimental

2.1. Chemicals

Thiamphenicol (100% purity) used as target pollutant was purchased from Sigma-Aldrich. In homogeneous processes, the solution pH was regulated with analytical grade sulfuric acid

supplied by Panreac, whereas analytical grade iron(II) sulfate heptahydrate used as catalyst was purchased from Merck. Anhydrous sodium sulfate used as supporting electrolyte was of analytical grade acquired from Merck. Ethanol and nitric acid, both of analytical grade, purchased from Panreac were used for pyrite washing. Standard carboxylic acids and other chemicals of analytical or high-performance liquid chromatography (HPLC) grade were supplied by Panreac and Merck. The electrolytic and analytical solutions were prepared with ultrapure water (resistivity > 18.2 MΩ cm) collected from a Millipore Milli-Q system.

2.2. Conditioning of pyrite catalyst

The natural pyrite used as heterogeneous catalyst was obtained from a mine located in northern Chile. It was milled with a ceramic mortar and further passed through a 200-mesh sieve, ensuring a particle size smaller than 80 μm. Fine particles and surface impurities were removed from the resulting powder by ultra-sonication in 95% ethanol for 5 min, followed by washing with 1 M HNO_3 solution and rinsing with Milli-Q water and 95% ethanol. Finally, the clean pyrite powder was dried at 30 ºC and kept in a desiccator.

2.3. Electrolytic assays

All electrolyses were performed in an open, undivided two-electrode cell containing 150 mL of a solution (homogeneous processes) or suspension (heterogeneous EF and PEF) under vigorous stirring with a magnetic follower. The solution temperature was regulated at 35 ºC by circulating thermostated water through a glass jacket. The anode was either an IrO_2-based (DSA®-O_2) plate purchased from NMT Electrodes or a BDD thin-film on Si acquired from NeoCoat. The cathode was a commercial carbon-PTFE air-diffusion electrode purchased from E-TEK. It was mounted in a tubular device as reported elsewhere (Steter et al., 2016), feeding it with compressed air flowing at 1 L min^{-1} for continuous H_2O_2 production. The geometric area of each electrode in contact with the solution was 3 cm^2 and the distance between the electrodes was kept at 1 cm in order to minimize the ohmic drop. The trials were always carried out under

145 galvanostatic conditions, with a constant *j* provided by an EG&G 363 potentiostat-galvanostat.
146 A Demestres 601 BR digital multimeter was employed to monitor the cell voltage. In PEF, the
147 solution was irradiated with a Philips TL/6W/08 fluorescent blacklight blue tube fixed at 7 cm
148 above the surface. The irradiance of this UVA lamp (λ_{max} = 365 nm) was of 5 W m^{-2}. All the
149 electrodes were first electrochemically activated and cleaned under electrochemical
150 polarization at j = 100 mA cm^{-2} for 240 min.

151 After each heterogeneous assay, the catalyst was recovered from the treated suspension by
152 filtration with paper, followed by several washing cycles with Milli-Q water and 95% ethanol
153 to assure the removal of all residues. Before starting each electrolysis in the presence of pyrite,
154 compressed air was bubbled through the suspension at 0.6 mL min^{-1} for 20 min using a diffusor,
155 thus reaching the dissolution equilibrium between pyrite and its dissolved ions. No adsorption
156 of thiamphenicol on pyrite occurred during such pre-treatment.

157 *2.4. Instruments and analytical procedures*

158 The surface morphology of pyrite was analyzed by field emission scanning electron
159 microscopy (FESEM) using a Carl Zeiss AG Supra 40 microscope. The composition was
160 studied by high-resolution transmission electron microscopy (HRTEM) using a JEOL JEM-
161 2100 LaB6 microscope, coupled to energy-dispersive X-ray spectroscopy (EDS) fulfilled with
162 an Oxford Instruments INCA x-sight detector. The elemental mapping was obtained with the
163 INCA Microanalysis Suite version 4.09 software. The chemical states of the elements in the
164 pyrite surface were analyzed by X-ray photoelectron spectroscopy (XPS) using a Physical
165 Electronics PHI 5500 Multitechnique System. The crystalline structure was elucidated by X-
166 ray diffraction (XRD) using a Bruker D8 ADVANCE diffractometer, with Cu K_α radiation (λ
167 = 1.5418 Å) and 2θ scan from 20° to 100° (at 1º min^{-1}).

168 A Crison GLP 22 pH-meter was utilized for pH measurements. For total organic carbon
169 (TOC) analysis, the samples were collected at regular time intervals and microfiltered (0.45

μm) with Whatman PTFE membrane filters before immediate analysis. TOC was monitored with a Shimadzu VCNS TOC analyzer by injecting a volume of 50 μL. The analysis was made with the non-purgeable organic carbon (NPOC) method, ensuring ± 1% accuracy.

The thiamphenicol concentration was determined by reversed-phase HPLC by injecting 20 μL aliquots into a Waters 600 liquid chromatograph coupled to a photodiode array detector set at λ = 225 nm (i.e., the wavelength of maximum absorption for the drug). The chromatograph was fitted with a BDS Hypersil C18 6 μm, 250 mm × 4.6 mm (i.d.), column at 25 °C, and a 50:50 (v/v) acetonitrile/water mixture was eluted at 1.0 mL min^{-1} as mobile phase. Upon sampling, dilution with acetonitrile was made to preserve the drug concentration. The peak related to thiamphenicol in the chromatograms appeared at a retention time (t_r) of 3.4 min. The same instrument, setting the detector at λ = 210 nm, was employed to quantify the short-chain carboxylic acids. For this, ion-exclusion HPLC analyses were carried out by fitting the instrument with a Supelcogel C610H, 30 cm × 7.8 mm (i.d.), column at 35 °C, using a 4 mM H_2SO_4 solution as the mobile phase eluted at 0.6 mL min^{-1}. The peaks appeared at t_r of 7.0 min for oxalic acid, 8.3 min for maleic acid, 9.4 min for oxamic acid, 13.7 min for formic acid and 14.9 min for fumaric acid.

Duplicate degradation and mineralization trials were made and average results are reported. In the figures, the error bars (95% confidence interval) have been added.

The H_2O_2 concentration was determined by spectrophotometry upon complexation with Ti(IV), since the resulting yellow solution absorbed at λ = 408 nm. A Shimadzu 1800 UV/Vis spectrophotometer at 35 ºC was employed (Welcher, 1975). The same instrument, selected at λ = 510 nm, was utilized for measuring the Fe^{2+} concentration from the light absorption of its reddish complex with 1,10-phenantroline. The released anions (Cl^-, SO_4^{2-} and NO_3^-) were analyzed by ion chromatography with a Shimadzu 10 Avp liquid chromatograph coupled with a Shimadzu CDD 10 Avp conductivity detector. The chromatograph was fitted with a Shim-

Pack IC-A1S, 100 mm × 4.6 mm (i.d.), anion column at 40 ºC and the mobile phase was composed of a 2.4 mM tris(hydroxymethyl)aminomethane and 2.5 mM phthalic acid mixture eluted at 1.5 mL min^{-1}. No NH_4^+ ion was detected upon analysis with a flow injection system (Thiam et al., 2016).

The primary by-products formed during the heterogeneous treatment of a suspension containing 50 mg L^{-1} thiamphenicol were detected by gas chromatography-mass spectrometry (GC-MS) following the same procedure reported elsewhere (Thiam et al., 2018). An Agilent Technologies system with a non-polar Agilent J&W HP-5 ms 0.25 μm, 30 m × 0.25 mm (i.d.), column was used and the identification was made by comparison with NIST05 MS database.

3. Results and discussion

3.1. Pyrite characterization

Fig. S1a-d show several FESEM images of the milled natural pyrite used as catalyst in this work, at different magnifications. As can be seen, the powder was composed of irregular microparticles, whose length varied between about 9 and 63 μm (see Fig. S1b). Their average size was 55 μm, thus becoming potentially adequate to carry out heterogeneous Fenton-based electrochemical treatments (Barhoumi et al., 2015). The shape of pyrite microparticles was confirmed by HRTEM at different magnifications, as shown in Fig. S2a and b. A selected microparticle observed at 8,000 × was analyzed by EDS, and the resulting spectrum is depicted in Fig. S3a. As expected, the EDS spectrum revealed the typical signals related to Fe and S, although much weaker peaks corresponding to C and O impurities appeared as well. The elemental analysis of a selected area of the microparticle (see Fig. S3b) evidenced a homogeneous distribution of Fe (see Fig. S3c) and S (see Fig. S3d) on its surface. From this analysis, the chemical composition of the sample was determined as: 44.8% Fe, 52.3% S, 1.95%

C and 0.95% O. These values are close to those of pure pyrite, which contains 46.5% Fe and 53.5% S.

The XPS spectrum given in Fig. 1a corroborates the presence of C and O in the pyrite sample. The high resolution spectra corresponding to Fe 2*p*, S 2*p*, C 1*s* and O 1*s* are presented in Fig. S4a-d, respectively. The former spectrum highlights the Fe $2p_{3/2}$ peak appearing at 707.0 eV, very close to 707.6 eV corresponding to the Fe(II)-S bond, and very different from 709.1 and 711.2 eV related to the Fe(III)-S and Fe(III)-O bonds, respectively (Herbert Jr. et al., 1998). Three peaks, at 168.4, 163.3 and 162.2 eV, can be observed in the high resolution spectrum of S $2p_{3/2}$ in Fig. S4b. They agree with the expected peak at 168.3-168.9 eV for alkali and alkaline-earth sulfates (Wahlqvist and Shchukarev, 2007), the 163.5 eV peak for polysulfide (S_n^{2-}) (Herbert Jr. et al., 1998) and the 162.3 eV peak for disulfide (Herbert Jr. et al., 1998). Fig. S4c highlights the signal at 283.9 eV related to C 1*s*, a value near 285.0 eV determined for a C-C/C-H bond, which allows discarding the presence of the –C=O bond of carbonate typically found at 289.0 eV (Greczynski and Hultman, 2020). Fig. S4d depicts a single peak at 531.3 eV in the O 1*s* spectrum, which agrees with the value of 531.2-531.9 eV reported for alkali and alkaline-earth sulfates (Wahlqvist, and Shchukarev, 2007). Therefore, these findings allow ascribing the impurities of C to organic compounds and those of O to sulfates.

Fig. 1b depicts the XRD pattern recorded for the natural pyrite, revealing the presence of very sharp peaks that suggest a high crystallinity. The pattern matched perfectly with the cubic structure of FeS_2, showing a cell parameter of a = 541.7 pm, based on the Joint Committee on Powder Diffraction Standards (JCPDS) card No. 42-1340. In this structure, the iron atoms are located in the vertices and center of the faces of the unit cell. The iron atoms and S_2^{2-} dimers occupy face-centered cubic (FCC) sites. Fig. 1b also shows the crystallographic planes associated with each peak in the FCC structure. The greater intensity corresponded to peaks at 33.1º and 56.3º, i.e., (211) and (311) planes, respectively.

3.2. Heterogeneous electro-Fenton treatment

First electrolytic assays were carried out to validate the ability of the stirred IrO_2/air-diffusion cell to accumulate H_2O_2 from cathodic O_2 reduction upon compressed air feeding, according to reaction (1). As an example, Fig. S5 depicts the evolution of H_2O_2 concentration during the electrolysis of 150 mL of a 0.020 M Na_2SO_4 solution at pH 3.0 and 35 ºC, working at j = 50 mA cm^{-2} for 360 min. A gradual increase in the content of this oxidant as time was prolonged can be observed, attaining the maximum accumulation of 49.1 mM at the end of the trial. However, the current efficiency calculated from the Faraday's law considering the stoichiometry of reaction (1) was halved, decreasing from a high value of 91.7% at 20 min (i.e., 5.7 mM of accumulated H_2O_2) down to a moderate value of 43.8% at 360 min. Such significant decay can be explained by the progressive enhancement of H_2O_2 direct oxidation to O_2 at the IrO_2 anode surface (Sirés et al., 2014; Coria et al., 2015). These results demonstrate the large ability of the electrolytic system to produce H_2O_2, which ensures the generation of sufficient $^{\bullet}OH$ species from Fenton's reaction (3) in the subsequent EAOPs for drug treatment.

In the literature, the relevant role played by pyrite dissolution regarding the medium acidification during Fenton-based treatments, according to reactions (7) and (8) (Barhoumi et al., 2015; Ouiriemmi et al., 2017), has been especially remarked. To confirm this phenomenon for the specific sample of natural pyrite prepared in this work, the Fe^{2+} concentration released in aqueous slurries containing a dose of 1.0, 2.0 and 3.0 g L^{-1} of conditioned mineral was monitored. Compressed air was bubbled through the suspension at a flow rate of 0.6 L min^{-1} to quickly attain the equilibrium between the pyrite microparticles and its dissolved ions, represented in reaction (7). Fig. S6a shows that, after 20 min, increasing steady Fe^{2+} concentrations of 0.021, 0.042 and 0.058 mM were already reached in each case. Based on these trends, we decided that prior to the application of the Fenton-based electrochemical treatments, a stabilization period of 20 min under air sparging through the suspension was

268 required, thus ensuring the maximum Fe^{2+} solubilization. In addition, the acidification of the
269 suspension during pyrite solubilization is also worth noticing. Fig. S6b depicts the rapid pH
270 decay when employing a dose of 1.0 g L^{-1} pyrite, changing from the initial value of 5.35 to 3.64
271 at 20 min, whereupon it remained constant. When Na_2SO_4 was added at a concentration of
272 0.020 M, the pH rose slightly up to 4.27, resulting from a small shift of reaction (7) to the left
273 due to the presence of more SO_4^{2-} ions. The same behavior was found for the other pyrite doses.

274 From the aforementioned considerations, the heterogeneous EF treatment of analogous
275 suspensions but in the presence of 50 mg L^{-1} thiamphenicol and 0.020 M Na_2SO_4 was performed
276 at j = 30 mA cm^{-2}. The initial pH in these tests, after 20 min of air bubbling, was of 4.27, 3.95
277 and 3.79 at 1.0, 2.0 and 3.0 g L^{-1} pyrite, respectively. Fig. 2a presents the inverse S-shape profile
278 found for the drug concentration decay at 1.0 g L^{-1} catalyst, attaining its total disappearance at
279 90 min. In contrast, exponential concentration abatements can be observed at 2.0 and 3.0 g L^{-1}
280 pyrite, with complete removal at 60 and 45 min, respectively. The greater degradation rate of
281 thiamphenicol at higher catalyst dosage can be ascribed to the larger production of oxidant $^{\bullet}OH$
282 from Fenton's reaction (3), owing to: (i) the higher Fe^{2+} release to the suspension (Fig. S6a),
283 and (ii) the lower initial pH, approaching the optimum pH of 3.0. According to this, the above
284 concentration decays were well fitted to a pseudo-first-order kinetics, as confirmed in the inset
285 of Fig. 2a. Table 1 summarizes the greater pseudo-first-order rate constant (k_1), with good R^2
286 values, obtained at higher catalyst content. This behavior suggests the generation of a small,
287 constant and increasing amount of $^{\bullet}OH$ in the above systems.

288 A similar enhancement of TOC removal, as the catalyst dose was increased, was found
289 when the heterogeneous EF treatment lasted for 360 min. Fig. 2b shows a poor mineralization
290 by this method since TOC was only abated by 17% and 35% at pyrite contents of 1.0 and 3.0 g
291 L^{-1} (see Table 1). The TOC decays were particularly decelerated from 120 min, which can be
292 explained by the formation of very stable by-products that are quite recalcitrant to the attack of

293 •OH. On the other hand, the fast Fe^{2+} generation from reaction (8) allows inferring the
294 predominance of this oxidation state for iron. The gradual acidification of the suspensions
295 during all the heterogeneous EF treatments (see Table 1) suggests the production of acid by-
296 products, like carboxylic acids, which are thus the main candidates to be complexed with Fe(II)
297 (and Fe(III)) and become quite refractory species (Brillas and Sirés, 2015).

298 The feasible adsorption of organic by-products formed from drug oxidation onto the
299 surface of pyrite microparticles was assessed by XRD analysis of the used catalyst, just
300 collected by filtration at the end of the electrolysis. Fig. 1c exemplifies the XRD pattern
301 recorded for the assay with 2.0 g L^{-1} pyrite. Comparison with Fig. 1b obtained for the natural
302 pyrite allows noticing a strong reduction of the relative intensity of the main signal (i.e., (200)
303 plane), which can be related to the presence of oxidation products blocking those sites. This
304 was supported by the fact that the same initial XRD pattern was recovered upon successive
305 rinsing of the collected catalyst with Milli-Q water and 95% ethanol. More specific recycling
306 tests are commented below.

307 The mineralization of thiamphenicol suspensions involves the accumulation of Cl^-, NO_3^-
308 and SO_4^{2-} ions, as discussed in subsection 3.5. The following theoretical reaction can then be
309 proposed for overall mineralization, with a number of consumed electrons n = 62:

310 $$C_{12}H_{15}Cl_2NO_5S + 26H_2O \rightarrow 12CO_2 + 2Cl^- + NO_3^- + SO_4^{2-} + 67H^+ + 62e^- \quad (10)$$

311 From this, the mineralization current efficiency (MCE, in %) for a given electrolytic assay
312 at current I (A) was determined from Eq. (11) (Sirés et al., 2014):

313 $$\text{MCE} = \frac{n\,F\,V\Delta\text{TOC}}{4.32\text{x}10^7 m\,I\,t}100 \quad (11)$$

314 where F is the Faraday constant, V is the solution volume (L), △TOC is the destroyed TOC
315 (mg L^{-1}), 4.32×10^7 is a homogenization factor (= 3600 s h^{-1} × 12000 mg C mol^{-1}), m is the
316 number of carbon atoms of the drug (= 12) and t is the electrolysis time (h).

317 The last column of Table 1 summarizes the MCE values calculated from Eq. (11) at the
318 end of the above heterogeneous EF tests. These values were quite low, evidencing the large
319 recalcitrance of thiamphenicol towards mineralization, and were slightly upgraded from 1.1%
320 to 2.2% when the pyrite content was risen from 1.0 to 3.0 g L^{-1}.

321 *3.3. Comparison of thiamphenicol removal by homogeneous and heterogeneous processes*

322 The oxidation power of the homogeneous and heterogeneous EF and PEF treatments of
323 150 mL of 50 mg L^{-1} of the drug in 0.020 M Na_2SO_4 was compared at j = 30 mA cm^{-2}. In
324 previous works using an air-diffusion cathode (Thiam et al., 2015; Steter et al., 2016; Alcaide
325 et al., 2020), 0.50 mM Fe^{2+} and pH close to 3 were determined as optimal for homogeneous
326 Fenton-based EAOPs. In the present study, the homogeneous EF and PEF treatments were
327 performed with a much lower value of 0.040 mM Fe^{2+}, similar to the value obtained upon
328 stabilization of pyrite at 2.0 g L^{-1} (see Fig. S6a), adjusting the initial pH to 3.0. Heterogeneous
329 EF and PEF were made with 2.0 g L^{-1} pyrite, at an initial pH of 3.95. The data of Table 1
330 evidence that the media became more acid in the four cases, in agreement with the typical
331 formation of acid by-products.

332 Fig. 3a shows the fast disappearance of thiamphenicol in the above processes. Its
333 concentration decay was slower in homogeneous EF, slightly quicker in heterogeneous EF and
334 much faster in both PEF treatments. Total drug disappearance occurred in 90, 75, 60 and 60
335 min, respectively. From the excellent linear profiles obtained from the corresponding pseudo-
336 first-order kinetic analysis shown in the inset of Fig. 3a, k_1-values varying between 0.0305 and
337 0.0347 min^{-1} under EF conditions and between 0.0396 and 0.0469 min^{-1} under PEF were found
338 (see Table 1). These findings suggest that the main oxidant was always the free $^{\bullet}OH$ formed
339 from Fenton's reaction (3), whereas the superiority of PEF over EF can be accounted for by the
340 production of additional amounts of this oxidant via photo-Fenton reaction (6) (Sirés et al.,
341 2014; Alcaide et al., 2020). In addition, when the homogeneous and heterogeneous modes are

compared either under EF or PEF conditions, the main factors affecting the performance are: (i) the extent to which reaction (8) is given, since it contributes to the continuous Fe^{2+} regeneration and the consequent acceleration of Fenton's reaction (3), and (ii) the additional production of •OH via heterogeneous Fenton's reaction (9).

These phenomena, along with the relative predominance of Fe(III) or Fe(II) species in the medium can justify the TOC-time profiles presented in Fig. 3b. Both EF treatments yielded a poor mineralization, with 26-31% of TOC removal at 360 min (see Table 1). This agrees with the generation of very persistent Fe(III) and/or Fe(II) complexes with some by-products in both cases. Since both trends were very similar, it can be concluded that Fenton's reaction (3) promoted by dissolved Fe^{2+} had a preeminent role as compared to heterogeneous reaction (9). In contrast, TOC was reduced by 54% in homogeneous PEF and to much larger extent (up to 85%) in heterogeneous PEF, with MCE values of 3.5% and 5.4%, respectively (see Table 1). In the homogeneous PEF treatment, the photolysis of recalcitrant Fe(III)-carboxylate complexes by UVA radiation via reaction (5) can justify the acceleration of mineralization as compared to EF. In the absence of a significant contribution of heterogeneous Fenton's reaction (9), as deduced from EF profiles, the much larger mineralization in heterogeneous PEF can be accounted for by the predominance of Fe^{2+} thanks to reaction (8). Worth noting, a more prolonged heterogeneous PEF treatment ensured the total mineralization in 450 min (not shown), thus avoiding secondary toxicity resulting from reaction products. The oxidation of the corresponding complexes with carboxylic acids is faster than that of Fe(III) complexes (Guelfi et al., 2019). It is then evident that the pyrite-catalyzed PEF process upgrades the mineralization of thiamphenicol, being a suitable EAOP for its degradation in water.

3.4. Effect of experimental variables on the heterogeneous photoelectro-Fenton performance

The influence of several key experimental variables on the performance of the heterogeneous PEF treatment of thiamphenicol was examined. A first study evaluated the role

of the anode by comparing the oxidation ability of electrolytic cells equipped with either an IrO_2-based or BDD one. Fig. S7a and its inset show a slight enhancement using BDD for the treatment of a suspension with 50 mg L^{-1} drug and 2.0 g L^{-1} pyrite at j = 30 mA cm^{-2}, as further confirmed by their k_1-values summarized in Table 1. Such an improvement can be ascribed to the higher oxidation power of the oxidant BDD(•OH) formed from reaction (2), being more active than IrO_2(•OH). However, the different electrocatalytic behavior was not relevant when addressing the drug mineralization. Fig. S7b evidences a similar TOC decay regardless of the anode material, attaining about 83-85% abatement (see Table 1). This means that the photolysis of by-products under irradiation with UVA light keeps the leading role in heterogeneous PEF. Moreover, BDD entails a larger investment and higher energy consumption, owing to the resulting greater cell voltage (E_{cell}) (see Table 1). The IrO_2 anode is thus preferable to operate a heterogeneous PEF system.

The effect of j, which determines the H_2O_2 production and •OH generation, was analyzed by electrolyzing suspensions containing 50 mg L^{-1} drug and 2.0 g L^{-1} pyrite at 15-50 mA cm^{-1}. Fig. S8a depicts the acceleration of the drug concentration decay at higher j, with complete disappearance after 75, 60 and 60 min at 15, 30 and 50 mA cm^{-2}, respectively, thanks to the concomitant acceleration of reactions (1)-(3). This is more evident from the increasing k_1-value, from 0.0250 to 0.0462 min^{-1}, based on the corresponding pseudo-first-order kinetic analysis of the inset of Fig. S8a. A different tendency can be observed in Fig. S8b for TOC removals. The mineralization increased largely when operating at 30 mA cm^{-2} instead of 15 mA cm^{-2}, meaning that the greater quantity of generated •OH accelerated the destruction of organics. In contrast, further increase to 50 mA cm^{-2} did not practically affect the TOC destruction. This confirms the crucial role of UVA light, since the mineralization of the final products is limited by their photodegradation rate, being the excess of •OH insufficient to promote their fast removal. Thus, j = 30 mA cm^{-2} was selected as optimal for this process. On the other hand, it is also worth

noting the gradual drop in MCE, from 7.9% at 15 mA cm^{-2} to 3.1% at 50 mA cm^{-2} (see Table 1). This decay is due to the larger relative loss of oxidant $^{\bullet}OH$ by the larger extent to which parasitic reactions occurred. These reactions included its reaction with H_2O_2 to yield the weaker oxidant hydroperoxyl radical ($HO_2^{\bullet}$) or with Fe^{2+} to give Fe^{3+} (Sirés et al., 2014).

The significant influence of parasitic reactions of $^{\bullet}OH$ on thiamphenicol degradation was also evidenced by varying the drug concentration between 5 and 75 mg L^{-1}, working at j = 30 mA cm^{-2}. Table 1 informs about the time for total drug abatement, which increased from 15 to 75 min, with decreasing k_1-values from 0.2459 to 0.0333 min^{-1}, within the above drug content range. However, for a suspension with 5 mg L^{-1} thiamphenicol, total removal occurred at 15 min, whereas a much greater content of 28 mg L^{-1} was degraded for a suspension with 75 mg L^{-1} drug (data not shown). This confirms the positive impact of drug content increase, which minimizes the parasitic reactions that cause the destruction of $^{\bullet}OH$.

Finally, the recyclability and reusability of pyrite as catalyst, without any cleaning step between successive trials, was tested in five consecutive cycles of heterogeneous PEF treatment of suspensions with 50 mg L^{-1} drug at j = 30 mA cm^{-2} for 360 min. Fig. 4a reveals a gradually lower decay of thiamphenicol concentration from the first to the fifth cycle. This can be better observed from Fig. 4b, where TOC reduction dropped from 85% in the first cycle to 47% in the last cycle. This confirm the adsorption of by-products onto the surface of pyrite microparticles, as described above from the XRD results of Fig. 1c. It seems then necessary to implement the cleaning procedure with Milli-Q water and 95% ethanol, in order to ensure the maximum activity of the catalyst in successive trials.

3.5. Identification of organic by-products and accumulated inorganic ions

The primary by-products of thiamphenicol accumulated during the heterogeneous Fenton-based EAOPs were identified by GC-MS after extraction of the residual organic components in the treated suspensions. In particular, suspensions containing 50 mg L^{-1} drug and 2.0 g L^{-1} pyrite

were treated by heterogeneous EF for 30 min at j = 30 mA cm^{-2}. The same by-products were formed in heterogeneous PEF because •OH is the main oxidant in both cases. Table S1 collects the chemical name, molecular structure, retention time and fragmentation ions of thiamphenicol (**1**), nine benzenic derivatives (compounds **2**, **4**-**8** and **10**-**12**) and two short-chain chlorinated aliphatics (compounds **3** and **9**) identified. Dechlorination, desulfonylation, hydroxylation, carboxylation/decarboxylation and the partial or complete loss of the lateral group of **1** are involved in the generation of the identified by-products.

The evolution of the final short-chain linear carboxylic acids identified during the heterogeneous EF and PEF treatments of suspensions with 50 mg L^{-1} thiamphenicol and 2.0 g L^{-1} pyrite at j = 30 mA cm^{-2} was monitored by ion-exclusion HPLC. Traces of maleic (**13**), fumaric (**14**) and formic (**17**) acids (< 0.1 mg L^{-1}) were detected, alongside much larger amounts of oxamic (**15**) and oxalic (**16**) acids. Maleic and fumaric acids arise from the cleavage of the benzenic ring of the aromatic by-products, whereas oxalic and formic acids come from the degradation of these two and other longer acids, and oxamic acid is derived from N-derivatives (Sirés et al., 2014). The three latter acids are directly mineralized to CO_2. Fig. 5a shows the continuous accumulation of oxalic acid, attaining up to 7.0 mg L^{-1} after 360 min in heterogeneous EF, but it is completely removed from the medium in heterogeneous PEF after reaching a maximal of 5.8 mg L^{-1} at 180-240 min of electrolysis. In contrast, Fig. 5b highlights a similar profile for oxamic acid in both processes, attaining a steady concentration near 3.6 mg L^{-1}. The large stability of oxalic acid in heterogeneous EF can be accounted for by the difficult oxidation of its Fe(II) and Fe(III) complexes, which are rapidly photolyzed in heterogeneous PEF. This justifies the superiority of the latter process in the TOC-time plots discussed above. Conversely, the recalcitrant Fe(II)- and Fe(III)-oxamate complexes remained stable under irradiation with UVA light. Hence, the inefficiency of this light to degrade this acid and other undetected by-products agrees with the partial mineralization observed in heterogeneous PEF

442 in previous subsections. A mass balance of generated carboxylic acids at the end of
443 heterogeneous EF reveals that they accounted for 2.8 mg L^{-1} TOC, only representing a 19% of
444 the 14.8 mg L^{-1} of residual TOC (see Fig. 4a). Therefore, a large proportion (around 81%) of
445 other very persistent by-products co-exists in the electrolyzed suspensions.

446 Ion chromatography analysis of the above suspensions (containing 0.140 mM drug)
447 revealed the almost overall release (> 97%) of its heteroatoms in the form of SO_4^{2-}, Cl^- and
448 NO_3^- ions. Fig. 5c exemplifies the time course of Cl^-, showing an analogous profile in
449 heterogeneous EF and PEF treatments. This ion was not oxidized to active chlorine because of
450 the low oxidation power of the IrO_2 anode (Thiam et al., 2015; Steter et al., 2016). In contrast,
451 Fig. 5d shows the large stability of accumulated NO_3^- in heterogeneous EF, and its progressive
452 removal in heterogeneous PEF since it is photolyzed to N_2 and O_2 (Halmann, 1996).

453 *3.6. Mineralization route of thiamphenicol by heterogeneous electrochemical processes*

454 Fig. 6 presents a reaction pathway proposed for thiamphenicol mineralization by
455 heterogeneous EF and PEF treatments with pyrite as heterogeneous catalyst and as a source of
456 homogeneous catalyst. The main oxidant is assumed to be $^{\bullet}OH$ formed from reaction (3) and/or
457 (6). Fe(II)- and Fe(III)-carboxylate complexes are not included, aiming to simplify the scheme.
458 The initial degradation of **1** involves four parallel pathways: (i) the partial cleavage of its lateral
459 group, yielding the sulfonyl benzene aldehyde derivative **2** and the dichloroaliphatic amine **3**;
460 (ii) its disulfonylation plus hydroxylation to yield compound **4**; and analogous reactions with
461 additional dechlorination, involving the loss of the Cl_2CH- group and carboxylation to form
462 either (iii) the compound **5** or (iv) **6**. Subsequent oxidation of **2** leads to the corresponding
463 benzoic acid **7**, which is dihydroxylated to yield **8**. Parallel oxidation of **3** yields the shorter
464 dichloroaliphatic amine **9**, which evolves to **15** to be mineralized to CO_2 and NO_3^- ion. In turn,
465 compounds **4** and **5** are transformed into **10** and **11**, respectively. These two latter by-products,
466 along with **6**, are then oxidized to the tetrahydroxylated benzoic acid **12**, which is accompanied

by the release of chloride and nitrate ions from different precursors. The cleavage of the benzene moiety of these aromatic by-products yields a mixture of the dicarboxylic acids **13** and **14**, which are then converted into **16** and **17**. These reactions, as well the mineralization of the two latter acids, occurs upon the slow action of •OH in heterogeneous EF, but much more rapidly through photodecarboxylation of complexed and free molecules in heterogeneous PEF, thus explaining the greater oxidation power of the photoassisted treatment.

4. Conclusions

It has been shown that natural pyrite can be successfully used for PEF treatment of thiamphenicol under UVA illumination. The mineral has a dual role, as solid catalyst to allow the heterogeneous Fenton's reaction and as a source of Fe^{2+} catalyst to promote the homogeneous Fenton's reaction. The oxidation profiles shown in this work have demonstrated the preponderance of the latter reaction. Pyrite acidifies the medium and releases dissolved Fe^{2+}, ensuring a very effective •OH production. The heterogeneous PEF treatment can be made with a cheap IrO_2-based anode, whose performance is similar to that of BDD. Comparative heterogeneous EF treatment yielded a similar disappearance of the antibiotic but a much slower mineralization because of the formation of persistent by-products. The mineralization power increased in the order: heterogeneous EF ~ homogeneous EF << homogeneous PEF << heterogeneous PEF. The Fe(II) complexes formed in heterogeneous PEF where quickly photolyzed, justifying the greater mineralization power. Under optimized operation conditions, 85% TOC abatement was achieved after 360 min. A detailed reaction route has been finally proposed, including the aromatic and aliphatic by-products identified. Pyrite-catalyzed PEF process seems an interesting alternative for the removal of drugs from water at natural pH.

Acknowledgements

The authors thank financial support from FONDECYT project 11180772 (CONICYT-Chile) and project CTQ2016-8616-R (AEI/FEDER, EU). We are also grateful to the program 'Becas Iberoamérica. Santander Universidades'.

References

Alcaide, F., Álvarez, G., Guelfi, D.R.V., Brillas, E., Sirés, I., 2020. A stable CoSP/MWCNTs air-diffusion cathode for the photoelectro-Fenton degradation of organic pollutants at pre-pilot scale. Chem. Eng. J. 379, 122417.

Barhoumi, N., Labiadh, L., Oturan, M.A., Oturan, N., Gadri, A., Ammar, S., Brillas, E., 2015. Electrochemical mineralization of the antibiotic levofloxacin by electro-Fenton-pyrite process. Chemosphere 141, 250-257.

Boye, B., Michaud, P.A., Marselli, B., Dieng, M.M., Brillas, E., Comninellis, C., 2002. Anodic oxidation of 4-chlorophenoxyacetic acid on synthetic boron-doped diamond electrode. New Diamond Frontier Carbon Technol. 12, 63-72.

Brillas, E., Sirés, I., 2015. Electrochemical removal of pharmaceuticals from water streams: Reactivity elucidation by mass spectrometry. TrAC-Trend. Anal. Chem. 70, 112-121.

Campos-Mañas, M.C., Plaza-Bolaños, P., Sánchez-Pérez, J.A., Malato, S., Agüera, A., 2017. Fast determination of pesticides and other contaminants of emerging concern in treated wastewater using direct injection coupled to highly sensitive ultra-high performance liquid chromatography-tandem mass spectrometry. J. Chromatogr. A 1507, 84-94.

Chu, W., Chu, T., Bond, T., Du, E., Guo, Y., Gao, N., 2016a. Impact of persulfate and ultraviolet light activated persulfate pre-oxidation on the formation of trihalomethanes, haloacetonitriles and halonitromethanes from the chlor(am)ination of three antibiotic chloramphenicols. Water Res. 93, 48-55.

513 Chu, W., Krasner, S.W., Gao, N., Templeton, M.R., Yin, D., 2016b. Contribution of the
514 antibiotic chloramphenicol and its analogues as precursors of dichloroacetamide and
515 other disinfection byproducts in drinking water. Environ. Sci. Technol. 50, 388-396.
516 Coria, G., Pérez, T., Sirés, I., Nava, J.L., 2015. Mass transport studies during dissolved oxygen
517 reduction to hydrogen peroxide in a filter-press electrolyzer using graphite felt, reticulated
518 vitreous carbon and boron-doped diamond as cathode. J. Electroanal. Chem. 757, 225-
519 229.
520 da Silva, L.M., Gozzi, F., Cavalcante, R.P., de Oliveira, S.C., Brillas, E., Sirés, I., Machulek
521 Jr., A., 2019. Assessment of 4-aminoantipyrine degradation and mineralization by
522 photoelectro-Fenton with a BDD anode: optimization, treatment in municipal secondary
523 effluent, and toxicity. ChemElectroChem 6, 865-875.
524 Deng, D., Deng, F., Tang, B., Zhang, J., Liu, J., 2017. Electrocatalytic reduction of low-
525 concentration thiamphenicol and florfenicol in wastewater with multi-walled carbon
526 nanotubes modified electrode. J. Hazard. Mater. 332, 168-175.
527 Ebele, A.J., Abou-Elwafa Abdallah, M., Harrad, S., 2017. Pharmaceuticals and personal care
528 products (PPCPs) in the freshwater aquatic environment. Emerg. Contam. 3, 1-16.
529 Expósito, E., Sánchez-Sánchez, C.M., Montiel, V., 2007. Mineral iron oxides as iron source in
530 electro-Fenton and photoelectro-Fenton mineralization processes. J. Electrochem. Soc.
531 154, E116-E122.
532 Fan, Y., Zheng, C., Hou, H., 2019. Preparation of granular activated carbon and its mechanism
533 in the removal of isoniazid, sulfamethoxazole, thiamphenicol, and doxycycline from
534 aqueous solution. Environ. Eng. Sci. 36, 1027-1040.
535 Feng, L., van Hullebusch, E.D., Rodrigo, M.A., Esposito, G., Oturan, M.A., 2013. Removal of
536 residual anti-inflammatory and analgesic pharmaceuticals from aqueous systems by
537 electrochemical advanced oxidation processes. A review. Chem. Eng. J. 228, 944-964.

Galia, A., Lanzalaco, S., Sabatino, M.A., Dispenza, C., Scialdone, O., Sirés, I., 2016. Crosslinking of poly(vinylpyrrolidone) activated by electrogenerated hydroxyl radicals: A first step towards a simple and cheap synthetic route of nanogel vectors. Electrochem. Commun. 62, 64-68.

Ganiyu, S.O., Zhou, M., Martinez-Huitle, C.A., 2018. Heterogeneous electro-Fenton and photoelectro-Fenton processes: a critical review of fundamental principles and application for water/wastewater treatment. Appl. Catal. B: Environ. 235, 103-129.

Ganzenko, O., Oturan, N., Sirés, I., Huguenot, D., van Hullebusch, E.D., Esposito, G., Oturan, M.A., 2018. Fast and complete removal of the 5-fluorouracil drug from water by electro-Fenton oxidation, Environ. Chem. Lett. 16, 281-286.

Ge, L., Chen, J., Qiao, X., Lin, J., Cai, X., 2009. Light-source-dependent effects of main water constituents on photodegradation of phenicol antibiotics: mechanism and kinetics. Environ. Sci. Technol. 43, 3103-3107.

Greczynski, G., Hultman, L., 2020. X-ray photoelectron spectroscopy: towards reliable binding energy referencing, Prog. Mater. Sci. 107, 100591.

Guelfi, D.R.V., Brillas, E., Gozzi, F., Machulek Jr., A., de Oliveira, S.C., Sirés, I., 2019. Influence of electrolysis conditions on the treatment of herbicide bentazon using artificial UVA radiation and sunlight. Identification of oxidation products. J. Environ. Manage. 231, 213-221.

Halmann, M.M., 1996. Photodegradation of Water Pollutants, CRC press, New York, 1996. Chapter II, p. 44.

He, J., Yang, X., Men, B., Wang, D., 2016. Interfacial mechanisms of heterogeneous Fenton reactions catalyzed by iron-based materials: A review. J. Environ. Sci. 39, 97-109.

Herbert Jr., R.B., Pratt, A.R., Blowes, D.W., Benner, S.G., 1998. Surface oxidation of iron monosulphide: an X-ray photoelectron spectroscopic study. Mineral. Mag. 62A, 608-609.

563 Kümmerer, K., Dionysiou, D.D., Olsson, O., Fatta-Kassinos, D., 2018. A path to clean water.
564 Science 361, 222-224.
565 Lanzalaco, S., Sirés, I., Sabatino, M.A., Dispenza, C., Scialdone, O., Galia, A., 2017. Synthesis
566 of polymer nanogels by electro-Fenton process: investigation of the effect of main
567 operation parameters. Electrochim. Acta 246, 812-822.
568 Li, K., Zhang, P., Ge, L., Ren, H., Yu, C., Chen, X., Zhao, Y., 2014. Concentration-dependent
569 photodegradation kinetics and hydroxyl-radical oxidation of phenicol antibiotics.
570 Chemosphere 111, 278-282.
571 Liu, M., Yin, H., Wu, Q., 2019. Occurrence and health risk assessment of pharmaceutical and
572 personal care products (PPCPs) in tap water of Shanghai. Ecotoxicol. Environ. Saf. 183,
573 109497.
574 Liu, N., Sijak, S., Zheng, M., Tang, L., Xu, G., Wu, M., 2015a. Aquatic photolysis of florfenicol
575 and thiamphenicol under direct UV irradiation, UV/H_2O_2 and UV/Fe(II) processes.
576 Chem. Eng. J. 260, 826-834.
577 Liu, W., Wang, Y., Ai, Z., Zhang, L., 2015b. Hydrothermal synthesis of FeS_2 as a high-
578 efficiency Fenton reagent to degrade alachlor via superoxide-mediated Fe(II)/Fe(III)
579 cycle. ACS Appl. Mater. Interf. 7, 28534-28544.
580 Marselli, B., Garcia-Gomez, J., Michaud, P.A., Rodrigo, M.A., Comninellis, C., 2003.
581 Electrogeneration of hydroxyl radicals on boron-doped diamond electrodes. J.
582 Electrochem. Soc. 150, D79-D83.
583 Mezzelani, M., Gorbi, S., Regoli, F., 2018. Pharmaceuticals in the aquatic environments:
584 evidence of emerged threat and future challenges for marine organisms. Mar. Environ.
585 Res. 140, 41-60.
586 Miller, T.H., Bury, N.R., Owen, S.F., MacRae, J.I., Barron, L.P., 2018. A review of the
587 pharmaceutical exposome in aquatic fauna. Environ. Pollut. 239, 129-146.

588 Ouiriemmi, I., Karrab, A., Oturan, N., Pazos, M., Rozales, E., Gadri, A., Sanromán, M.A.,
589 Ammar, S., Oturan, M.A., 2017. Heterogeneous electro-Fenton using natural pyrite as
590 solid catalyst for oxidative degradation of vanillic acid. J. Electronal. Chem. 797, 69-77.
591 Özcan, A., Özcan, A.A., Demirci, Y., Şener, E., 2017. Preparation of Fe_2O_3 modified kaolin
592 and application in heterogeneous electro-catalytic oxidation of enoxacin. Appl. Catal. B:
593 Environ. 200, 361-371.
594 Panizza, M., Cerisola, G., 2009. Direct and mediated anodic oxidation of organic pollutants.
595 Chem. Rev. 109, 6541-6569.
596 Panizza, M., Oturan, M.A., 2011. Degradation of Alizarin Red by electro-Fenton process using
597 a graphite-felt cathode. Electrochim. Acta 56, 7084-7087.
598 Pérez, T., Sirés, I., Brillas, E., Nava, J.L., 2017. Solar photoelectro-Fenton flow plant modeling
599 for the degradation of the antibiotic erythromycin in sulfate medium. Electrochim. Acta
600 228, 45-56.
601 Prieto-Rodríguez, L., Oller, I., Klamerth, N., Agüera, A., Rodríguez, E.M., Malato, S., 2013.
602 Application of solar AOPs and ozonation for elimination of micropollutants in municipal
603 wastewater treatment plant effluents. Water Res. 47, 1521-1528.
604 Scialdone, O., Galia, A., Randazzo, S., 2011. Oxidation of carboxylic acids in water at IrO_2-
605 Ta_2O_5 and boron doped diamond anodes. Chem. Eng. J. 174, 266-274.
606 Sirés, I., Brillas, E., Oturan, M.A., Rodrigo, M.A., Panizza, M., 2014. Electrochemical
607 advanced oxidation processes: today and tomorrow. Environ. Sci. Pollut. Res. 21, 8336-
608 8367.
609 Steter, J.R., Brillas, E., Sirés, I., 2016. On the selection of the anode material for the
610 electrochemical removal of methylparaben from different aqueous media. Electrochim.
611 Acta 222, 1464-1474.

612 Thiam, A., Brillas, E., Centellas, F., Cabot, P.L., Sirés, I., 2015. Electrochemical reactivity of
613 Ponceau 4R (food additive E124) in different electrolytes and batch cells. Electrochim.
614 Acta 173, 523-533.
615 Thiam, A., E. Brillas, E., Garrido, J.A., Rodríguez, R.M., Sirés, I., 2016. Routes for the
616 electrochemical degradation of the artificial food azo-colour Ponceau 4R by advanced
617 oxidation processes. Appl. Catal. B: Environ. 180, 227-236.
618 Thiam, A., Salazar, R., Brillas, E., Sirés, I., 2018. Electrochemical advanced oxidation of
619 carbofuran in aqueous sulfate and/or chloride media using a flow cell with a RuO_2-based
620 anode and an air diffusion cathode at pre-pilot scale. Chem. Eng. J. 334, 133-144.
621 Wahlqvist, M., Shchukarev, A., 2007. XPS spectra and electronic structure of Group IA
622 sulfates. J. Electron Spectrosc. Relat. Phenom. 156-158, 310-314.
623 Wang, F., Wang, W., Yuan, S., Wang, W., Hu, Z.-H., 2017. Comparison of UV/H_2O_2 and
624 UV/PS processes for the degradation of thiamphenicol in aqueous solution. J. Photochem.
625 Photobiol. A: Chem. 348, 79-88.
626 Welcher, F.J. (ed.), 1975. Standard Methods of Chemical Analysis, vol. 2, Part B, 6th ed., R.E.
627 Krieger Publishers, Huntington, New York, p. 1827.
628 Yang, W., Zhou, M., Oturan, N., Li, Y., Su, P., Oturan, M.A., 2019. Enhanced activation of
629 hydrogen peroxide using nitrogen doped graphene for effective removal of herbicide 2,4-
630 D from water by iron-free electrochemical advanced oxidation. Electrochim. Acta 297,
631 582-592.
632 Ye, Z., Brillas, E., Centellas, Cabot, P.L., Sirés, I., 2019. Electro-Fenton process at mild pH
633 using Fe(III)-EDDS as soluble catalyst and carbon felt as cathode. Appl. Catal. B:
634 Environ. 257, 117907.

635 Ye, Z., Brillas, E., Centellas, Cabot, P.L., Sirés, I., 2020. Expanding the application of
636 photoelectro-Fenton treatment to urban wastewater using the Fe(III)-EDDS complex.
637 Water Res. 169, 115219.
638 Yin, K., Deng, L., Luo, J., Crittenden, J., Liu, C., Wei, Y., Wang, L., 2018. Destruction of
639 phenicol antibiotics using the UV/H_2O_2 process: kinetics, byproducts, toxicity evaluation
640 and trichloromethane formation potential. Chem. Eng. J. 351, 867-877.
641 Zhang, P., Huang, W., Ji, Z., Zhou, C., Yuan, S., 2018. Mechanisms of hydroxyl radicals
642 production from pyrite oxidation by hydrogen peroxide: surface versus aqueous reactions.
643 Geochim. Cosmochim. Acta 238, 394-410.
644 Zhang, Y., Tran, H.P., Hussain, I., Zhong, Y., Huang, S., 2015. Degradation of *p*-chloroaniline
645 by pyrite in aqueous solutions. Chem. Eng. J. 279, 396-401.
646 Zheng, M., Daniels, K.D., Park, M., Nienhauser, A.B., Clevenger, E.C., Li, Y., Snyder, S.A.,
647 2019. Attenuation of pharmaceutically active compounds in aqueous solution by
648 UV/CaO_2 process: influencing factors, degradation mechanism and pathway. Water Res.
649 164, 114922.

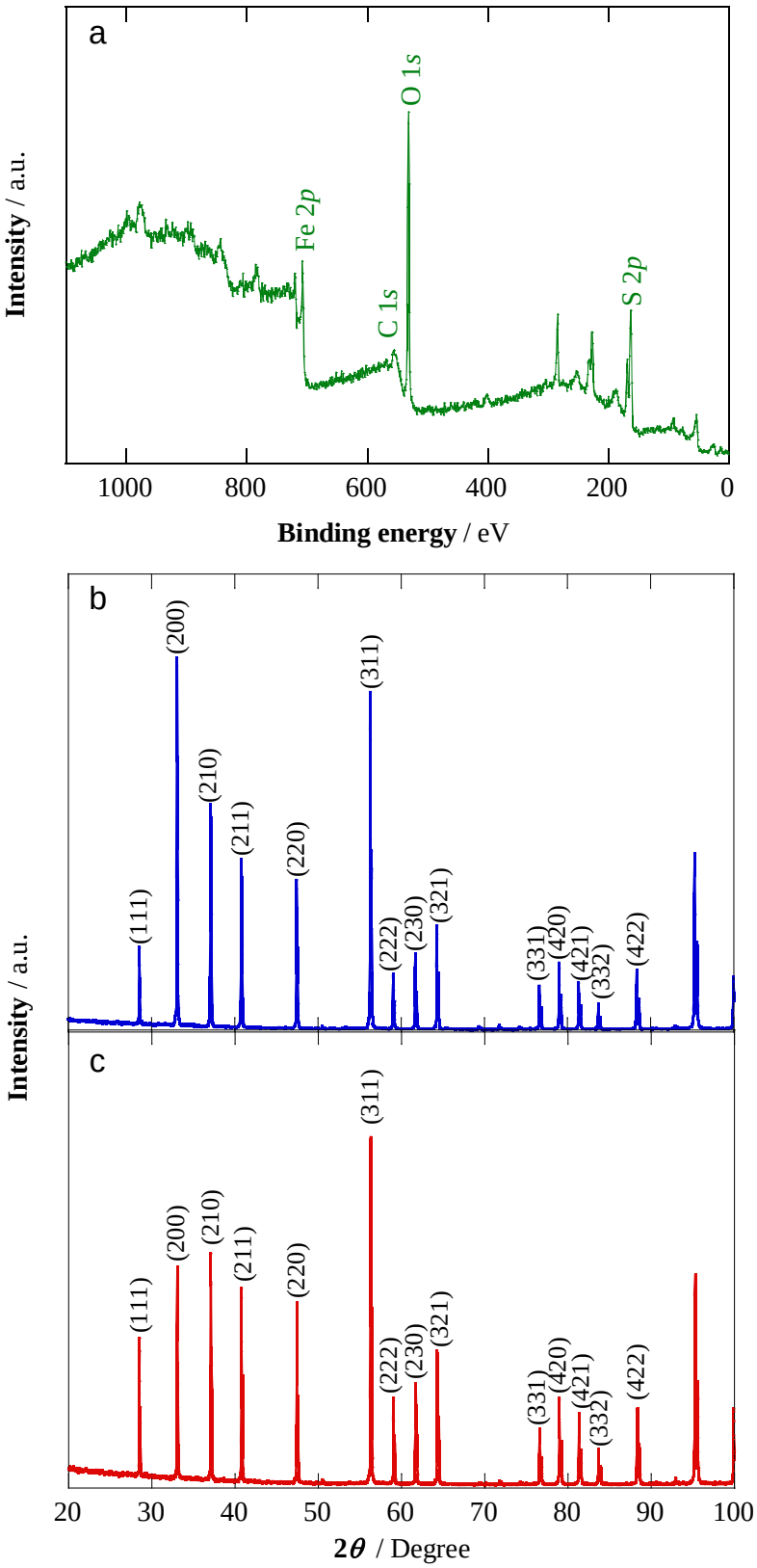

Fig. 1. (a) General XPS spectrum of natural pyrite. XRD pattern of natural pyrite: (a) initial and (b) recovered after the heterogeneous EF treatment of a suspension with 50 mg L^{-1} thiamphenicol, 0.020 M Na_2SO_4 and 2.0 g L^{-1} pyrite at pH 3.95 and 35 ºC, using an IrO_2/air-diffusion cell at a current density (j) of 30 mA cm^{-2}.

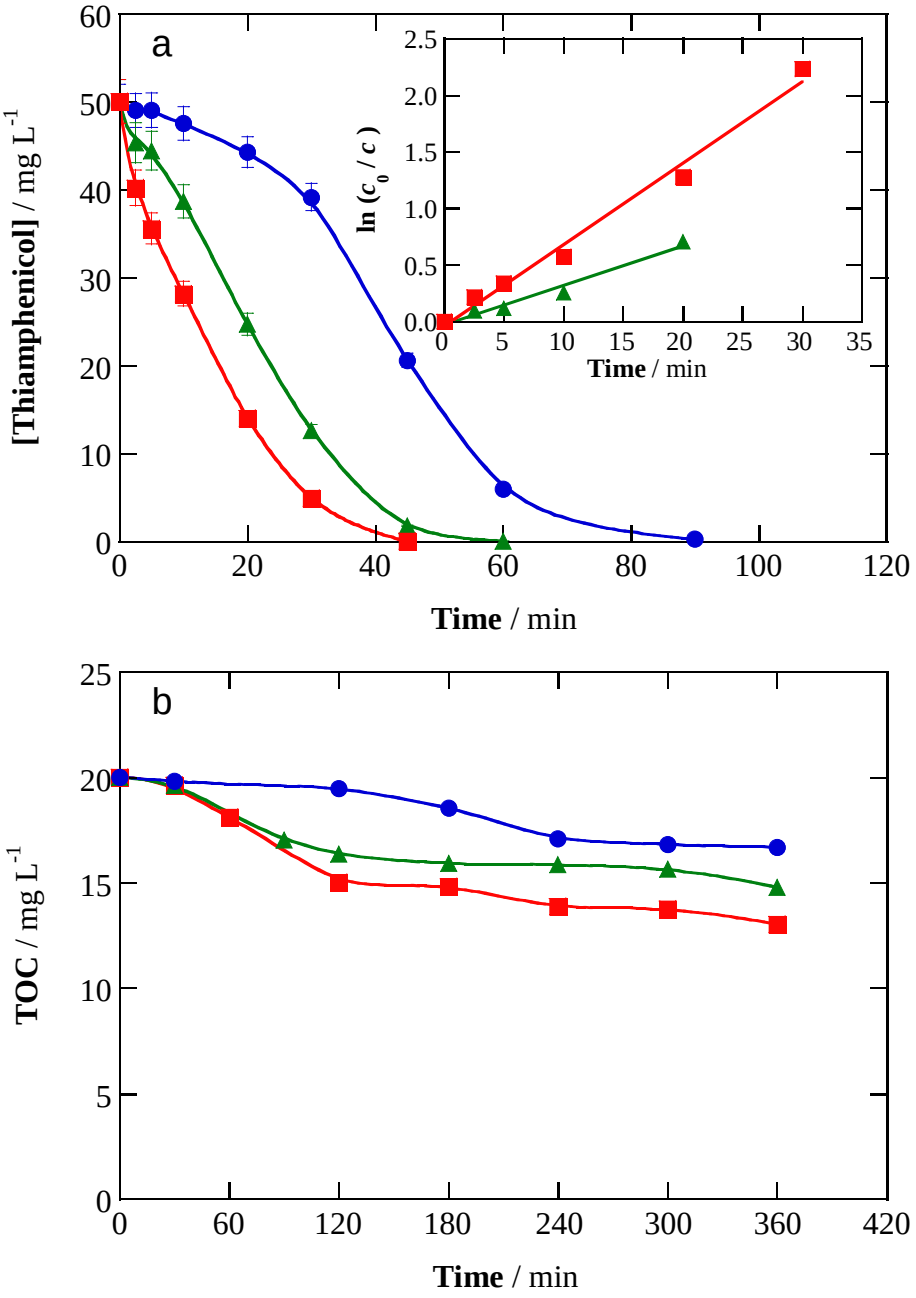

Fig. 2. Effect of pyrite content on (a) thiamphenicol concentration abatement, along with the pseudo-first-order kinetic analysis, and (b) TOC removal vs. electrolysis time for the heterogeneous EF treatment of 150 mL of a suspension containing 50 mg L^{-1} (0.140 mM) thiamphenicol and 0.020 M Na_2SO_4 at 35 ºC, using a stirred IrO_2/air-diffusion cell at j = 30 mA cm^{-2}. Pyrite content: (●) 1.0 g L^{-1} (initial pH 4.27), (▲) 2.0 g L^{-1} (initial pH 3.95) and (■) 3.0 g L^{-1} (initial pH 3.79).

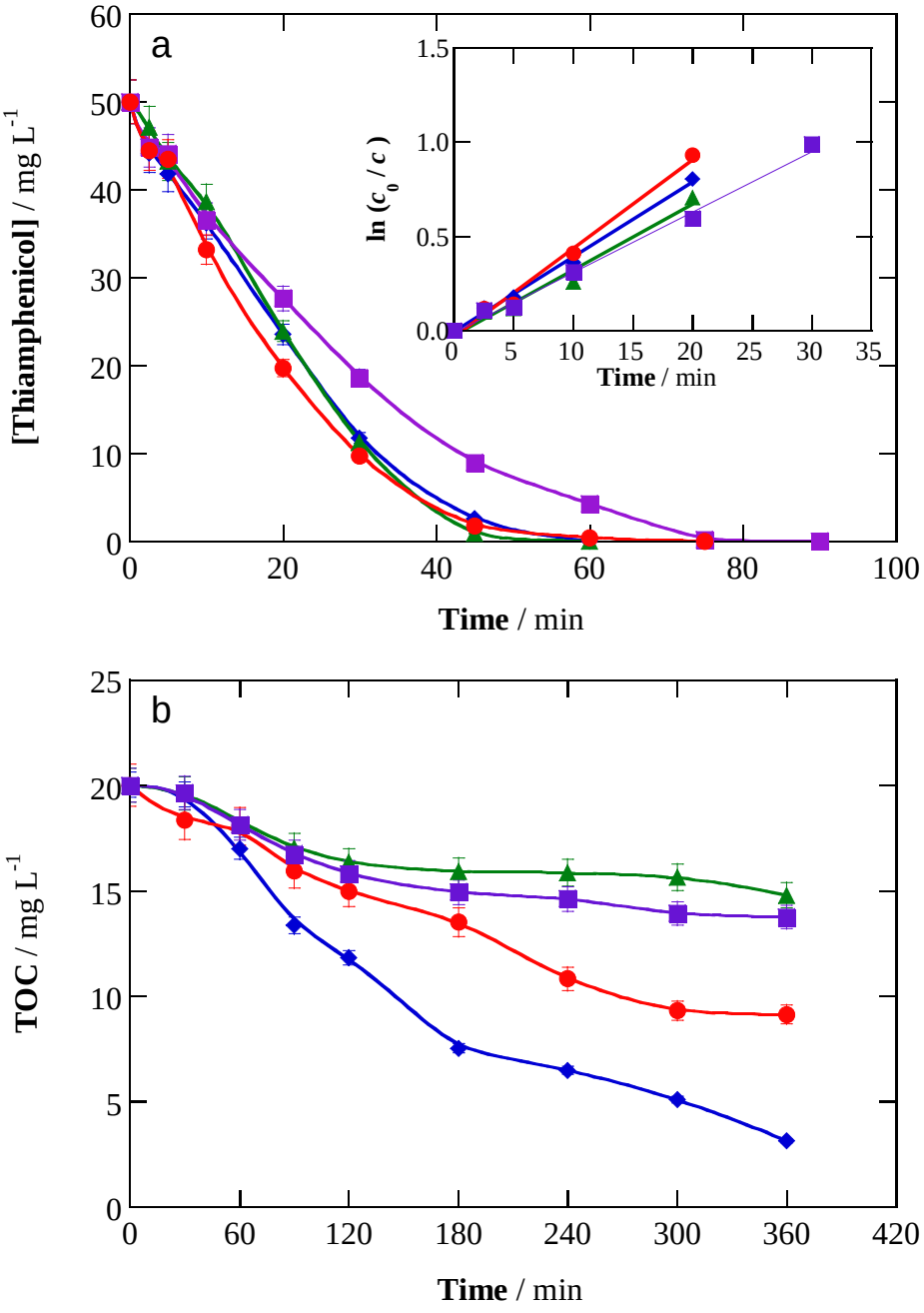

Fig. 3. (a) Thiamphenicol concentration decay, along with the pseudo-first-order kinetic analysis, and (b) TOC removal vs. time for the electrolysis of 150 mL of 50 mg L^{-1} drug in 0.020 M Na_2SO_4 at 35 ºC, using a stirred IrO_2/air-diffusion cell at j = 30 mA cm^{-2}. Treatment: Homogeneous (■) EF and (●) PEF with 0.40 mM Fe^{2+} at pH 3.0; heterogeneous (▲) EF and (◆) PEF with 2.0 g L^{-1} pyrite at initial pH 3.95.

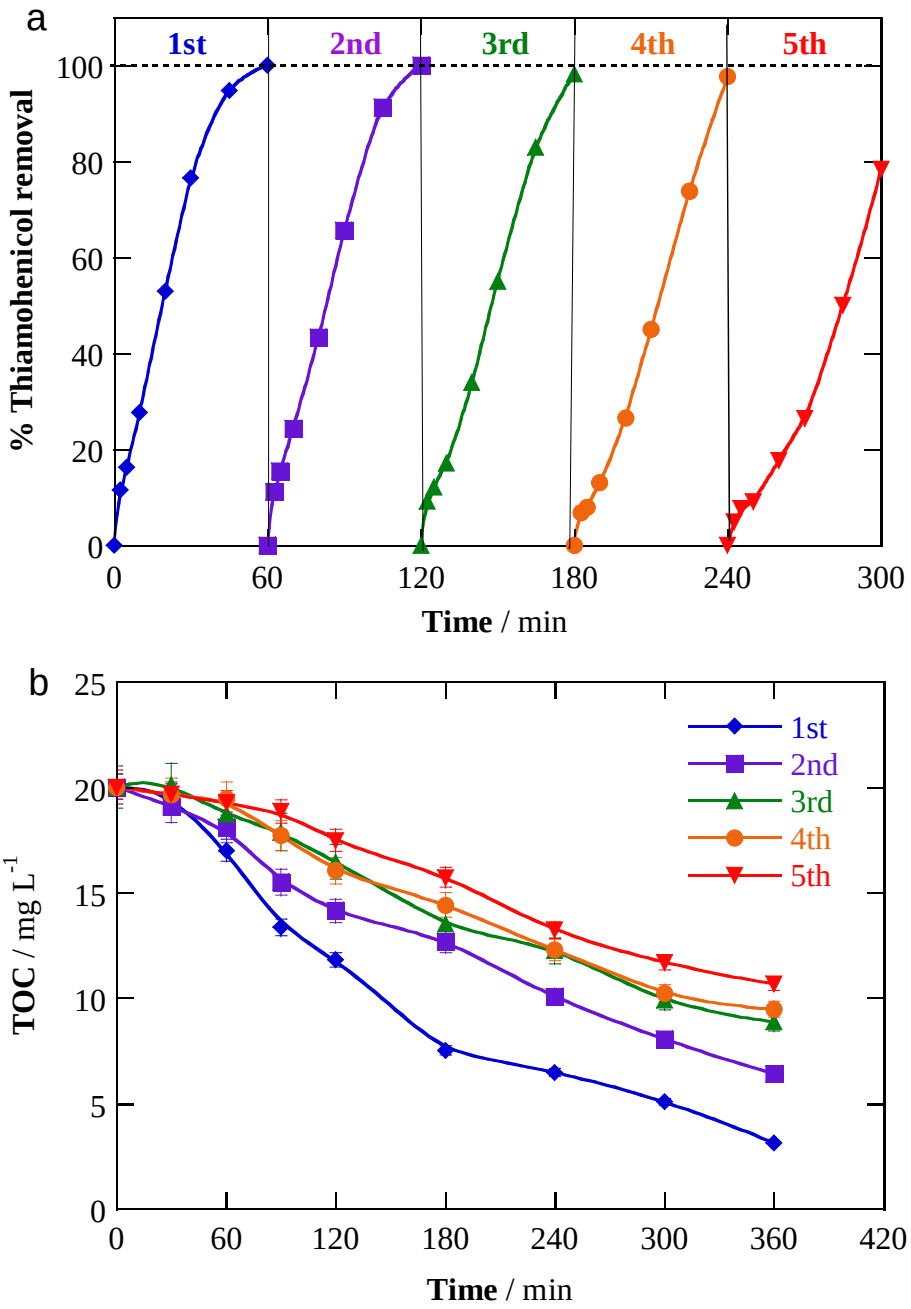

Fig. 4. Time course of (a) the percentage of thiamphenicol removal and (b) TOC versus electrolysis time for the heterogeneous PEF treatment of 150 mL of suspensions containing 50 mg L^{-1} drug, 0.020 M Na_2SO_4 and 2.0 g L^{-1} pyrite at initial pH 3.95 and 35 ºC, using a stirred IrO_2/air-diffusion cell at j = 30 mA cm^{-2} upon 5 consecutive cycles.

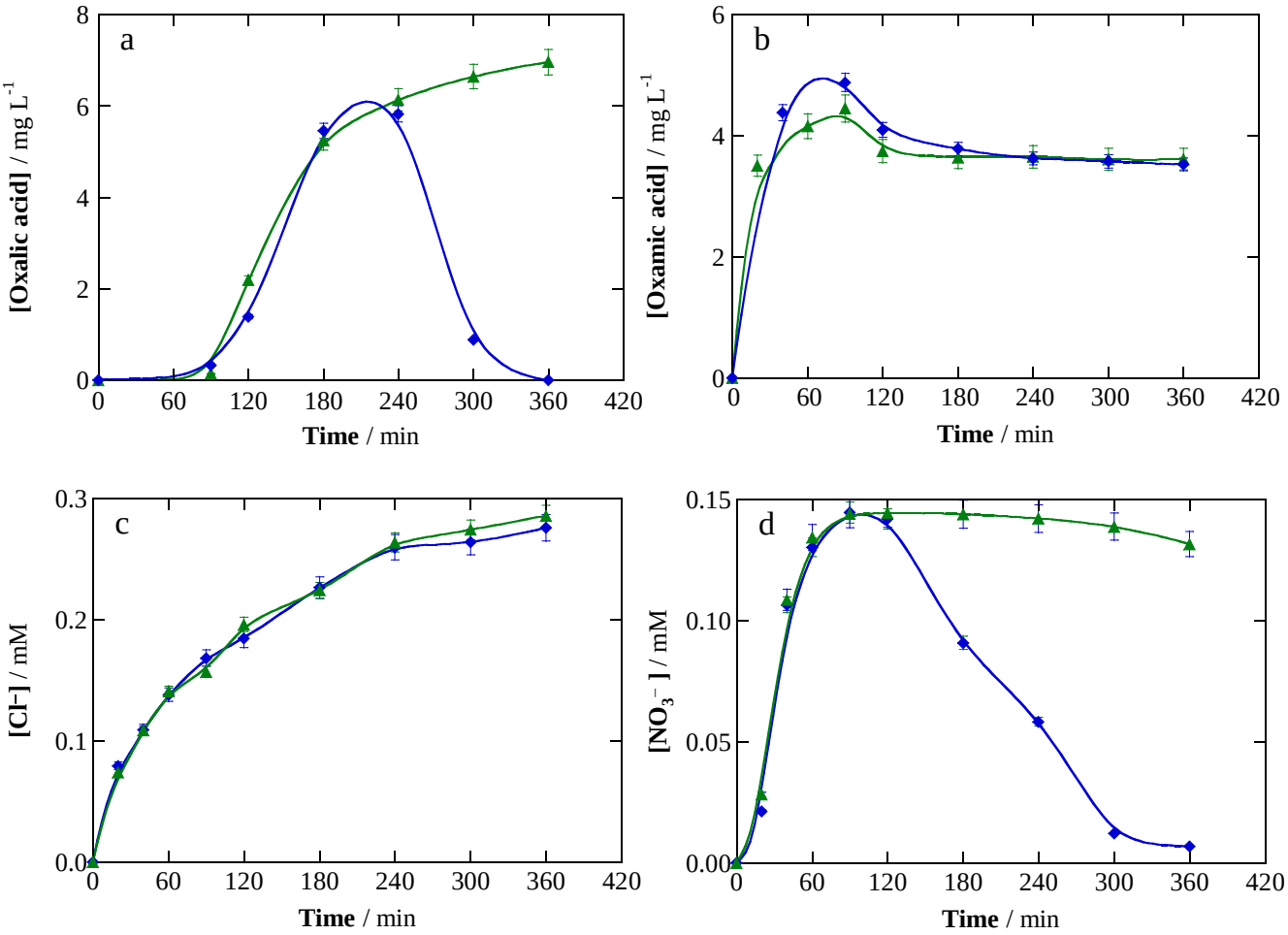

Fig. 5. Time course of the concentration of (a) oxalic acid, (b) oxamic acid, (c) chloride ion and (d) nitrate ion detected during the heterogeneous (▲) EF and (◆) PEF treatments of 150 mL of suspensions containing 50 mg L^{-1} drug, 0.020 M Na_2SO_4 and 2.0 g L^{-1} pyrite at initial pH 3.95 and 35 ºC, using a stirred IrO_2/air-diffusion cell at j = 30 mA cm^{-2}.

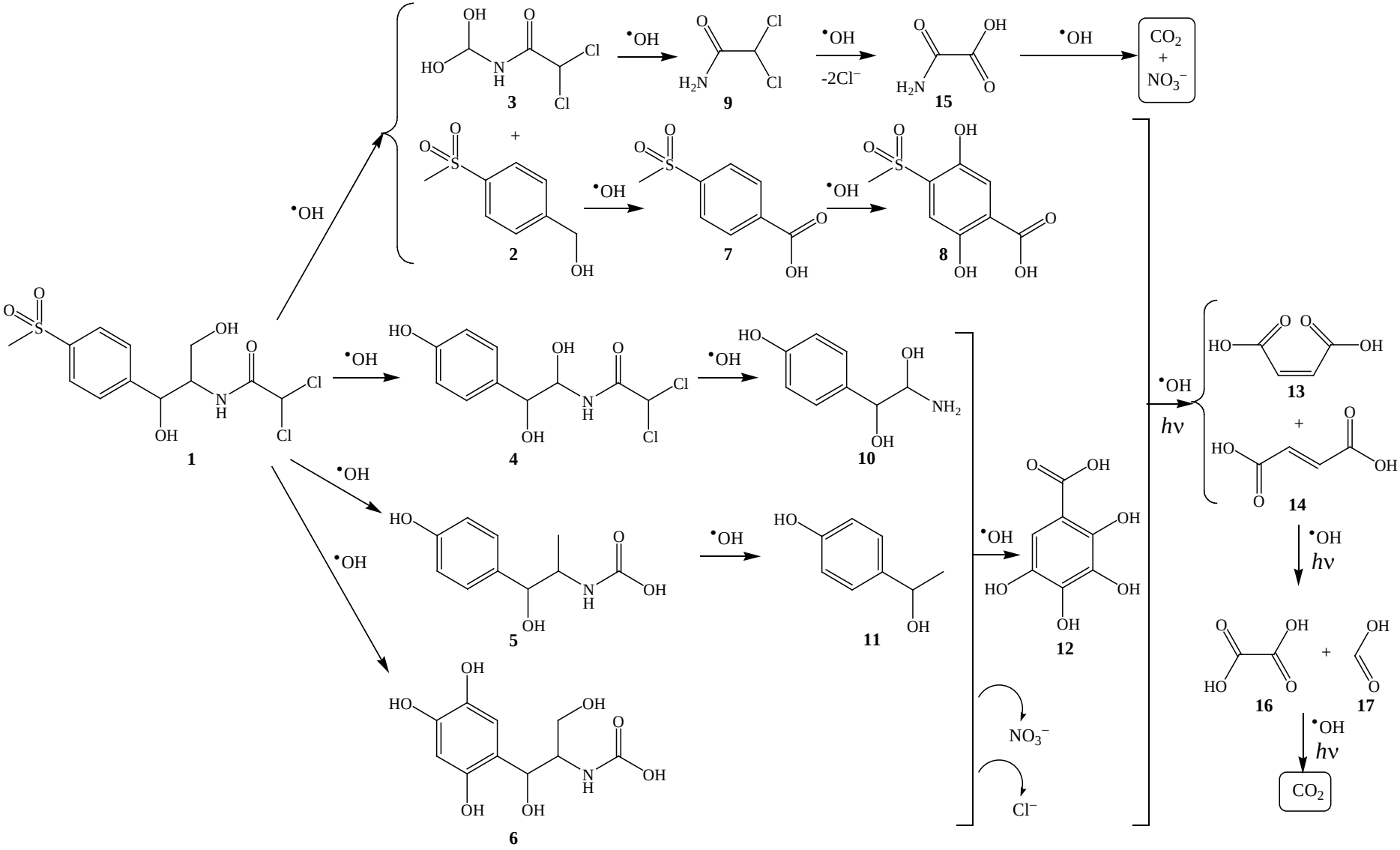

Fig. 6. Proposed reaction pathway for the mineralization of thiamphenicol (**1**) by heterogeneous EF and PEF treatments.

Table 1

Main results obtained for the homogeneous and heterogeneous EF and PEF treatments of thiamphenicol solutions/suspensions in 0.020 M Na_2SO_4 under different conditions using an air-diffusion cathode.

Anode	[Thiamphenicol] (mg L^{-1})	[Fe^{2+}] (mM)	[Pyrite] (g L^{-1})	j [a] (mA cm^{-2})	E_{cell} [b] (V)	Initial pH (final pH)[c]	Time for total drug decay (min)	k_1 [d] (min^{-1})	R^2	% TOC removal at 360 min	% MCE at 360 min
Homogeneous EF											
IrO_2	50	0.040	-	30	9.4	3.00 (2.83)	90	0.0305	0.979	31	2.0
Heterogeneous EF											
IrO_2	50	-	1.0	30	10.5	3.79 (2.65)	90	-	-	17	1.1
IrO_2	50	-	2.0	30	9.3	3.95 (2.50)	60	0.0347	0.973	26	1.7
IrO_2	50	-	3.0	30	8.7	4.27 (2.45)	45	0.0719	0.987	35	2.2
Homogeneous PEF											
IrO_2	50	0.040	-	30	9.6	3.00 (2.91)	75	0.0469	0.986	54	3.5
Heterogeneous PEF											
IrO_2	5	-	2.0	30	9.3	3.95 (2.74)	15	0.2459	0.987	- [e]	- [e]
IrO_2	10	-	2.0	30	9.2	3.95 (2.69)	30	0.1049	0.987	- [e]	- [e]
IrO_2	25	-	2.0	30	9.1	3.95 (2.73)	45	0.1465	0.993	- [e]	- [e]
IrO_2	50	-	2.0	15	5.6	3.95 (2.70)	90	0.0250	0.993	62	7.9
BDD	50	-	2.0	30	14.7	3.95 (2.32)	45	0.0426	0.998	83	5.3
IrO_2	50	-	2.0	30	9.1	3.95 (2.69)	60	0.0396	0.994	85	5.4
IrO_2	50	-	2.0	50	14.3	3.95 (2.78)	55	0.0462	0.989	82	3.1
IrO_2	75	-	2.0	30	9.3	3.95 (2.80)	75	0.0333	0.998	- [e]	- [e]

[a] Current density. [b] Average cell voltage. [c] In heterogeneous process, pyrite was added to the drug + Na_2SO_4 solution (pH 5.35) and air was bubbled for 20 min to attain the dissolution equilibrium of the catalyst. [d] Pseudo-first-order rate constant for thiamphenicol. [e] Not determined.